Tunable Resistance or Magnetoresistance Cusp and Extremely Large Magnetoresistance in Defect-Engineered $HfTe_{5-\delta}$ Single Crystals

Yang-Yang Lv,[1] Xiao Li,[2] Lin Cao,[1] Dajun Lin,[1] Shu-Hua Yao,[1,3,*] Si-Si Chen,[2] Song-Tao Dong,[4] Jian Zhou,[1,3] Y. B. Chen,[2,†] and Yan-Feng Chen[1,3]

[1]*National Laboratory of Solid State Microstructures and Department of Materials Science and Engineering, Nanjing University, Nanjing 210093, China*
[2]*National Laboratory of Solid State Microstructures and Department of Physics, Nanjing University, Nanjing 210093, China*
[3]*Collaborative Innovation Center of Advanced Microstructure, Nanjing University, Nanjing 210093, China*
[4]*Institute of Materials Science and Engineering, Jiangsu University of Science and Technology, Zhenjiang 212003, China*

(Received 17 November 2017; revised manuscript received 8 March 2018; published 31 May 2018)

The electrical transport behaviors of novel materials under the external magnetic field B, especially the large or tunable magnetoresistance (MR) effect, are of broad importance in both fundamental science and applications. Here three kinds of $HfTe_5$ crystals with varied Te-deficiency concentrations are synthesized under different growth conditions, and they demonstrate distinct electrical and magnetotransport properties. The temperatures of the resistivity cusp or MR cusp of the as-grown $HfTe_{5-\delta}$ ($\delta = 0.02, 0.08, 0.13$) crystals are tuned from 25 to 90 K. The maximum MR of these three $HfTe_{5-\delta}$ crystals, under 2 K and 9 T B, are $1.52 \times 10^3\%$, $2.63 \times 10^4\%$, and $6.91 \times 10^3\%$ for sample SI ($HfTe_{4.98}$), SII ($HfTe_{4.92}$), and SIII ($HfTe_{4.87}$), respectively. The fitting of Hall data by the two-carrier model suggests that the extremely large MR effect of sample $HfTe_{4.92}$ measured at 2 K is attributed to the cooperative action of the high mobility and the coexistence of the electron and hole carriers. Our work provides a viable route to tune superior MR properties in similar compounds through defect engineering, which may be promising to develop magnetic memory sensor devices.

DOI: 10.1103/PhysRevApplied.9.054049

I. INTRODUCTION

In recent years, the extremely large magnetoresistance (XMR) effect, much larger than the giant MR (GMR) effect in a magnetic multilayer [1] and the colossal MR (CMR) in a manganite perovskite [2], was discovered in some *non-magnetic* materials [3–17]. The XMR effect has attracted tremendous interest because of both potential applications in modern electronic devices [18–20] and its underlying physical origins. Up to now, several possible physical mechanisms leading to XMR have been proposed. For example, the XMR in bismuth [3], graphite [4], $PtSn_4$ [7], Mo/WTe_2 [9,12], $NbSb_2$ [10], LaSb [11], and $PtBi_2$ [13] is reported to arise from perfect electron-hole balance. But, the recent angle-resolved photoemission spectroscopy works substantiate that the electron-hole compensation in WTe_2 occurs only in a narrow temperature range, and the concentration of hole carriers is higher than that of electron carriers in $MoTe_2$ [21,22], which also is suggested in the electrical transport studies of Zandt *et al.* [23]. The results violate the nearly electron-hole compensation picture in Mo/WTe_2. And more, the observed XMR of $PdCoO_2$ is closely related to the high carrier mobility and there are only hole carriers [8]. Shen *et al.* claimed that a synergetic action of a substantial difference between electron and hole mobility, as well as a moderate carrier compensation, leads to the XMR in YSb [24]. These discoveries provide valuable clues on how to tailor materials to obtain the XMR property.

$HfTe_5$, being a member of nonmagnetic layered materials, has been known for several decades [25]. $HfTe_5$ demonstrates the mysterious resistivity cusp [26–28], pronounced quantum oscillations [29,30], large thermopower [31,32], unusual topological matters [33–36], pressure-driven superconductivity [37,38], and high carrier mobility [36,39,40]. Among them, the most remarkable phenomenon is the resistivity cusp at the resistivity-temperature curve, accompanied by the change in sign of the thermopower or Hall coefficient (phenomenologically, the major carrier changes from an electron to a hole). The underlying physical origin is still under hot debate [41–43]. Recently, some experimental

*Corresponding author.
shyao@nju.edu.cn
†Corresponding author.
ybchen@nju.edu.cn

 © 2018 American Physical Society

and theoretical works claimed that the resistivity cusp is attributed to electron-hole compensation, where the hole is the intrinsic carrier, and the electron carrier may come from Te deficiency [44] or topology-protected surface states [39]. The high carrier mobility and the potential electron-hole compensation in $HfTe_5$ could make it a promising material platform to achieve the XMR property. It is noteworthy that samples grown by different methods show the resistivity anomaly at different temperatures (50–80 K) [36–40,44]. These results suggest that we can tailor the concentration of Te deficiency during the growth process to manipulate the electrical and magnetotransport properties of $HfTe_5$.

Taking this ideal into account, we grow three batches of $HfTe_{5-\delta}$ crystals with various deficient Te concentrations by adding different excessive amounts of Te in the vapor transport growth process. To simplify the discussion, the as-grown crystals are denoted as SI, SII, and SIII hereafter, respectively. A composition analysis substantiates that the chemical ratios Hf/Te are 1.00∶4.98, 1.00∶4.92, and 1.00∶4.87 in SI, SII, and SIII, respectively. These $HfTe_{5-\delta}$ crystals show the temperature of the resistivity or magnetoresistance cusp at 25(/70), 51(/80), and 72(/90) K, respectively. The maximum MR values, measured at 2 K and 9 T magnetic field (B), are $1.52 \times 10^3\%$, $2.63 \times 10^4\%$, and $6.91 \times 10^3\%$ for SI ($HfTe_{4.98}$), SII ($HfTe_{4.92}$), and SIII ($HfTe_{4.87}$) samples, respectively. Fitting the Hall data verifies that the MR cusp observed in MR-temperature curves and the extremely large MR effect in $HfTe_{4.92}$ measured at 2 K may be attributed to the high carrier mobility and the coexistence of the electron and hole carriers. Our results suggest that the defect engineering in the growth process is effective to tune the MR behavior in the $HfTe_5$ system. This viable route can be transferable to other transition-metal compounds to achieve the XMR effect in these compounds and, thus, provide versatile platforms to develop magnetosensor and magnetoactuator devices [18–20]. It should be mentioned that sometimes magnetosensor or -actuator applications need the materials working at different temperature windows. Our work described as follows demonstrates that the resistivity cusp or MR cusp of defect-engineered $HfTe_{5-\delta}$ can be tuned from 25 to 90 K, which maybe widens the working temperatures of corresponding devices based on $HfTe_5$.

II. EXPERIMENT

Similar to the previous reports [25,36], three kinds of $HfTe_5$ single crystals are synthesized by a chemical vapor transport (CVT) technique with I_2 as the transport agent and adding extra Te. The schematic of the CVT setup is shown in Fig. 1(a). In a typical run, $HfTe_5$ powder is first prepared by a solid-state reaction. The stoichiometric (1∶5) mixture of Hf (Strem 99.999%) and Te (Alfa Aesar 99.999%) powders are heated at 773 K for several days in the evacuated and sealed quartz tube of 25 mL in volume. Then, several grams $HfTe_5$ powders together with about 5 $mg\,cm^{-3}$ of I_2 powder (Alfa Aesar 99.999%) and extra Te powder (3% for SI, 1% for SII, and 0% for SIII, respectively) are ground and loaded into another evacuated quartz tube and placed in a two-zone furnace to grow crystals. Afterward, the ampoule is put to a temperature gradient from 773 to 673 K for 10 days and finally cooled down naturally to room temperature. The as-grown single crystals are characterized on an x-ray diffractometer (XRD, Ultima III Rigaku) using Cu-K_α radiation with 2θ of 10°–70° to investigate the crystal orientation. Single-crystal data are collected at 300 K on a Gemini S Ultra x-ray diffractometer (Oxford diffraction) with Mo-K_α radiation ($\lambda = 0.71073$ Å). Structure refinement is carried out with the program SHELXL-2014/7 implemented in the program suite Apex 3. An energy-dispersive x-ray spectroscopy (EDS) detector equipped with a scanning electron microscope (SEM) (FEI-Quanta) is used to determine the chemical composition. The electrical transport measurements for the roughly rectangular crystals are performed on a Quantum Design physical properties measurement system (QD PPMS-9 T) employing the standard six-probe method by the current injected along the a axis, the longest dimension of these crystals.

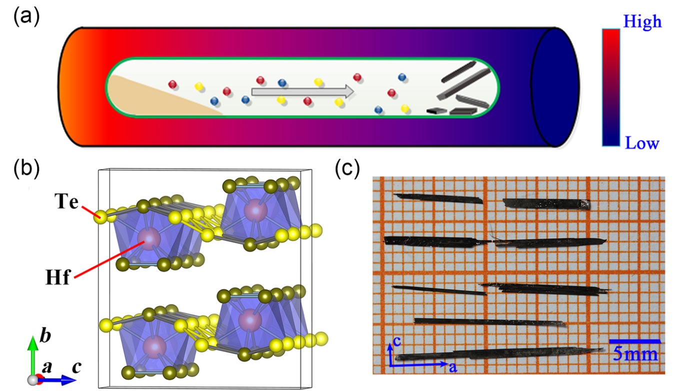

FIG. 1. (a) The schematic of the CVT growth equipment and the growth process of $HfTe_{5-\delta}$ single crystals. (b) The crystal structure of $HfTe_5$. (c) The typical photograph of the as-grown $HfTe_{5-\delta}$ single crystals.

III. RESULTS AND DISCUSSION

As depicted in Fig. 1(b), the layered material $HfTe_5$ is adopted in an orthorhombic structure with the space group $Cmcm$. In the structure of $HfTe_5$, trigonal prismatic $HfTe_3$ chains connected by a zigzag Te-Te chain form a two-dimensional (2D) $HfTe_5$ layer in the ac plane, and 2D $HfTe_5$ layers are stacked along the b axis to form a ribbonlike crystal. Figure 1(c) presents the optical picture of $HfTe_{5-\delta}$ crystals. Obviously, the series of $HfTe_{5-\delta}$ crystals show metallic luster with the size up to $20 \times 1 \times 0.5$ mm^3. The as-grown crystals can be well preserved by the dry air for several months.

The XRD patterns of the maximum exposed surface of single-crystal SI samples are shown in Fig. 2(a) (black

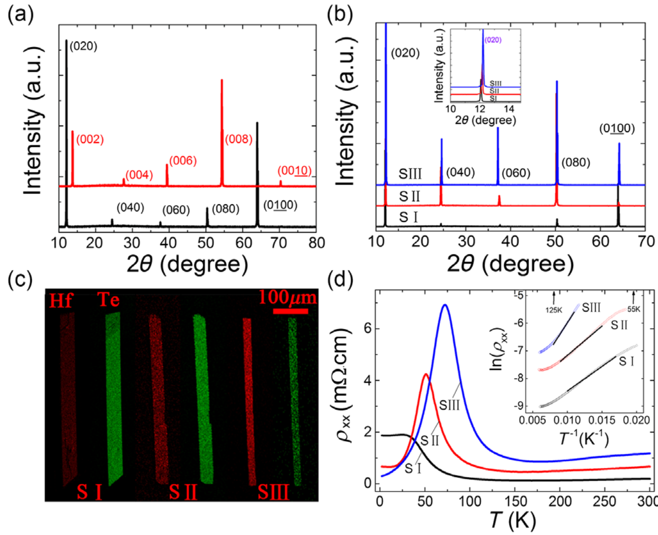

FIG. 2. (a) XRD patterns of the representative SI ($HfTe_{4.98}$) single crystals measured on the *ac* and *ab* planes, respectively. Other two samples have similar XRD patterns. (b) XRD patterns of the *ac* plane for samples SI ($HfTe_{4.98}$), SII ($HfTe_{4.92}$), and SIII ($HfTe_{4.87}$), respectively. The inset is the enlarged (020) XRD peaks for all samples. The abbreviation "a. u." denotes arbitrary units. (c) Hf (red) and Te (green) element mapping images of samples SI ($HfTe_{4.98}$), SII ($HfTe_{4.92}$), and SIII ($HfTe_{4.87}$), respectively. (d) Temperature-dependent resistivity ρ_{xx} of $HfTe_5$ crystal samples SI ($HfTe_{4.98}$), SII ($HfTe_{4.92}$), and SIII ($HfTe_{4.87}$), respectively. The insets show $\ln \rho_{xx}$ as a function of T^{-1}. The open symbols represent the experiment data, and the black lines show the linear fit.

pattern). All peaks can be indexed as (0 2*k* 0) reflections, which suggests that the exposed sample surface belongs to the *b* plane. Using the same method, the *c* plane is also substantiated by XRD measurements. In order to show the effect of growth conditions on the crystal structure, we plot the XRD patterns [Fig. 2(b)] of the *b* plane for SI, SII, and SIII, respectively. The full width at half maximum of series $HfTe_{5-\delta}$ samples (002-pole) varies from 0.06° to 0.08°, which infers the as-grown single crystals have a high crystalline quality. It also displays that the diffraction peaks gradually shift to a higher angle from SI to SIII [see the inset in Fig. 2(b)]. To show the change of lattice parameters, we collect and refine the single-crystal XRD data for all crystals. The obtained unit-cell parameters are $a = 3.9742$ (3.9714, 3.9698) Å, $b = 14.5058$ (14.4470, 14.4016) Å, $c = 13.7500$ (13.7237, 13.7013) Å, and $V = 792.68$ (787.42, 783.32) Å^3 for SI (SII, SIII) samples, respectively. Their differences may originate from the composition differences. Figure 2(c) depicts the EDS mappings of Hf and Te elements in SI, SII, and SIII samples, respectively. The EDS analysis indicates that the chemical compositions of the as-grown crystals are Hf : Te = 1.00 : 4.98, 1.00 : 4.92, and 1.00 : 4.87 for SI, SII, and SIII, respectively. These results suggest that the introduction of extra Te composition would reduce the concentration of Te deficiency. Figure 2(d) displays the temperature (T) dependence of resistivity ρ, in the T range from 2 to 300 K under a zero magnetic field, for the three different $HfTe_{5-\delta}$ ($\delta = 0.02$, 0.08, 0.13) crystals. It should be mentioned that the ρ-T curves for SI ($HfTe_{4.98}$), SII ($HfTe_{4.92}$), and SIII ($HfTe_{4.87}$) shown here are reproducible by checking several crystals synthesized in the same growth condition. As shown in Fig. 2(d), the ρ-T behavior of samples $HfTe_{4.92}$ and $HfTe_{4.87}$ is quite similar. For example, they all show metallic behavior at a temperature range from 170 to 300 K, then there is a resistivity cusp from 40 to 170 K, and they do the metallic feature again from 2 to 40 K. Different from these samples, sample $HfTe_{4.98}$ shows metallic behavior from 170 to 300 K, a semiconductinglike behavior from 40 to 170 K, and then a steplike feature below 30 K, and certainly ρ of sample $HfTe_{4.98}$ has a faint cusp around 25 K. In addition, evidently, the temperature of the resistivity cusp of $HfTe_{4.98}$, $HfTe_{4.92}$, and $HfTe_{4.87}$ is at 25, 51, and 72 K, respectively. These data demonstrate the tenability of the resistivity cusp in defect-engineered $HfTe_5$ crystals. To understand the charge conduction mechanism, we apply the Arrhenius equation $[\rho_{xx} = \rho_0 \exp[\Delta/(\kappa_b T)]]$ to analyze the semiconductinglike behavior of the samples at a temperature range from 125 to 55 K. As plotted in the inset in Fig. 2(d), the linear behavior of $\ln \rho_{xx}$ vs $(1/T)$ is observed in these three samples. The energy gap Δ is extracted as 15, 18, and 32 meV for $HfTe_{4.98}$, $HfTe_{4.92}$, and $HfTe_{4.87}$, respectively, which is comparable to the earlier reports [39,44]. The difference between $HfTe_{4.98}$, $HfTe_{4.92}$, and $HfTe_{4.87}$ indicates the energy barrier for hole excitation will increase with the introduction of more Te defects.

We further characterize the magnetotransport properties of these $HfTe_{5-\delta}$ samples. Figures 3(a)–3(c) plot the B dependence of longitudinal MR under variable temperatures for the samples SI ($HfTe_{4.98}$), SII ($HfTe_{4.92}$), and SIII ($HfTe_{4.87}$), respectively. As shown in Figs. 3(a) and 3(b), in the samples $HfTe_{4.98}$ and $HfTe_{4.92}$, the MR is sublinearly dependent on B under a low field at the measured temperature range. Different from the two samples, in the MR-B curve of the sample $HfTe_{4.87}$, an obvious peak at about 1.8 T is observed at 2 K. And the peak position shifts toward the high field with an increased temperature and disappears at $T > 20$ K in our measured range. The origin of the anomalous MR peak is still elusive [45,46], which will be further studied in the near future. To demonstrate MR behaviors of these samples clearly, we plot the MR-T curves under 9-T B for these three samples in Fig. 3(d). For the sample $HfTe_{4.98}$, the saturated MR reaches $1.52 \times 10^3\%$ at 9 T and 2 K. With a rising temperature, its MR initially increases gradually and then exhibits an unsaturated maximum MR ($4.62 \times 10^3\%$) centered around $T_{P\text{-}S1} = 70$ K, upon which the MR decreases gradually again with an increasing temperature before reaching 32% under 9-T B at room temperature. Different from $HfTe_{4.98}$, the MR for sample $HfTe_{4.92}$

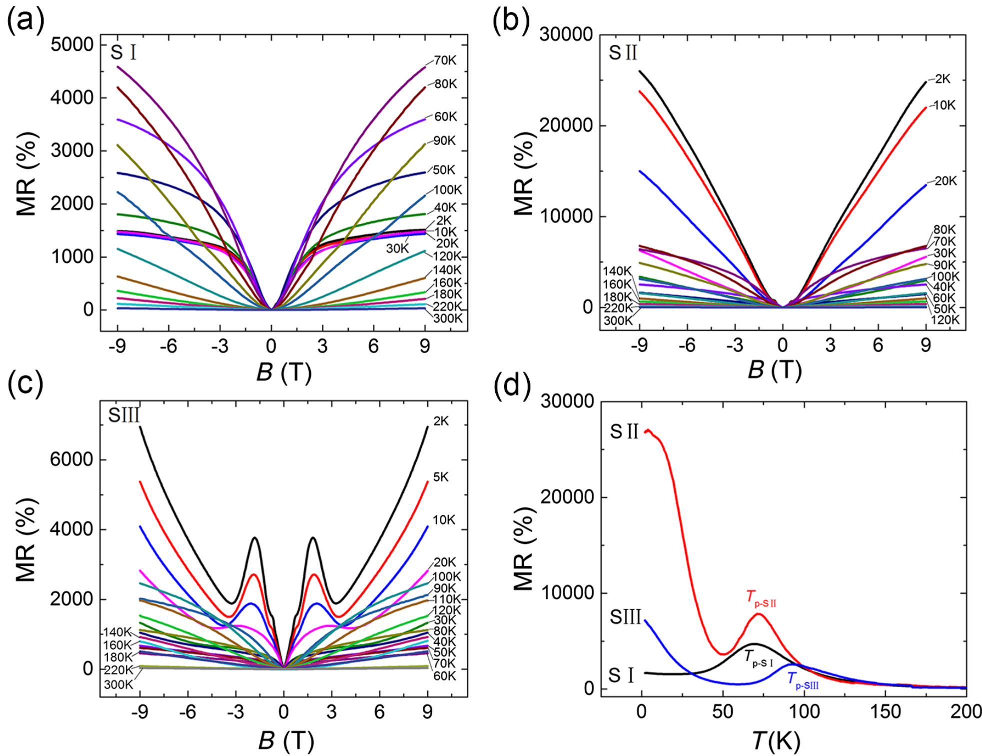

FIG. 3. The relationship between MR and magnetic field B of samples SI ($HfTe_{4.98}$) (a), SII ($HfTe_{4.92}$) (b), and SIII ($HfTe_{4.87}$) (c), under several temperatures, with B applied along the b axis and scanned from 0 to 9 T. (d) Temperature-dependent MR measured at 9 T for samples SI ($HfTe_{4.98}$), SII ($HfTe_{4.92}$), and SIII ($HfTe_{4.87}$), respectively.

[see Fig. 3(b)] is unsaturated at 2 K with its maximum as $2.63 \times 10^4\%$ at 9 T and 2 K and then decreased with elevating temperature. At about 50 K, the minimum MR is reached, $1.51 \times 10^3\%$ at 9-T B. And above this temperature, the MR gradually increases upon heating up to a peak value at $T_{P\text{-}S2} = 80$ K, upon which the MR decreases as the temperature rises and finally reaches 33% at 9-T B at room temperature. The MR behavior of sample $HfTe_{4.87}$ measured under 9-T B is similar to $HfTe_{4.92}$ [see Fig. 2(d)]. Obviously, the MR under 9-T B reaches a maximum value of $6.91 \times 10^3\%$ at 2 K, a minimum value of $4.52 \times 10^2\%$ at about 60 K, a peak value of $2.54 \times 10^3\%$ at about $T_{P\text{-}S3} = 90$ K, and 31% at room temperature. It should be emphasized that, in the sample $HfTe_{4.92}$, the maximum MR value, measured at 2 K and 9 T magnetic field, reaches up to $2.63 \times 10^4\%$, which is the highest value reported for any ideal two-dimensional (2D) transition-metal chalcogenides so far, to the level of the XMR effect in the previous studies of some 3D systems ($PtSn_4$, $PdCoO_2$, Mo/WTe_2, $NbSb_2$, LaSb, and $PtBi_2$, etc. [7–13]). In short, the magnetotransport properties of $HfTe_{5-\delta}$ are strongly dependent on Te-defect concentration.

To understand the above-mentioned electrical and magnetotransport behavior in $HfTe_{5-\delta}$ crystals, we conduct Hall measurements. As shown in Figs. 4(a)–4(c), all samples $HfTe_{5-\delta}$ ($\delta = 0.02$, 0.08, and 0.13, respectively) show nonlinear Hall curves at the temperature ranges from 2 to 300 K, which suggests the relationship between Hall resistivity and B should be analyzed by the classical two-carrier model [47]. For sample $HfTe_{4.98}$ [Fig. 4(a)], the slope of Hall resistivity is negative at a low field (<1 T) and then turns positive in a high-field regime (>1 T) below 60 K. On the contrary, the slope of Hall resistivity changes from positive at a low field (<1 T) to negative at a high field (>1 T) with T within 60–70 K. At temperatures above 80 K, the Hall coefficients are always positive in the field regime (0–9 T). Phenomenologically, the main carrier changes from electrons to holes dependent on the temperature. Sample $HfTe_{4.92}$ [Fig. 4(b)] shows a similar trend to $HfTe_{4.98}$. At 2 K, the Hall coefficient changes from negative to positive at about 3 T. And it also turns to be positive at a low field (<2 T) at 60 K. Above 70 K, the Hall coefficient is always positive in the whole field regime. Different from above-mentioned two samples, the Hall coefficient of sample $HfTe_{4.87}$ [Fig. 4(c)] is negative and has a trough at about 1.5 T at 2 K. Compared with the MR-B of sample $HfTe_{4.87}$, the anomalous trough may be correlated to MR peaks shown in Fig. 3(c) nearly at the same B. The Hall coefficient changes from negative to positive as the temperature ranges from 2 to 300 K, similar to $HfTe_{4.98}$ and $HfTe_{4.92}$. It turns to be positive at a low field (<1 T) at 80 K and then be positive in the whole field regime above 90 K.

We further analyze quantitatively the Hall data by the two-carrier model (fitting curves are shown in Fig. 5). Figures 4(d)–4(f) present the temperature-dependent carrier concentrations and mobility, extracted from the fitting of samples SI ($HfTe_{4.98}$), SII ($HfTe_{4.92}$), and SIII ($HfTe_{4.87}$), respectively. As shown in Fig. 4(d), at a low temperature (<70 K), the two kinds of carriers in the sample $HfTe_{4.98}$ are both electronlike carriers which may come from different electronic bands [36,48]. At 2 K, the carrier density is estimated to be $n_1 = 1.23 \times 10^{18}\ \text{cm}^{-3}$

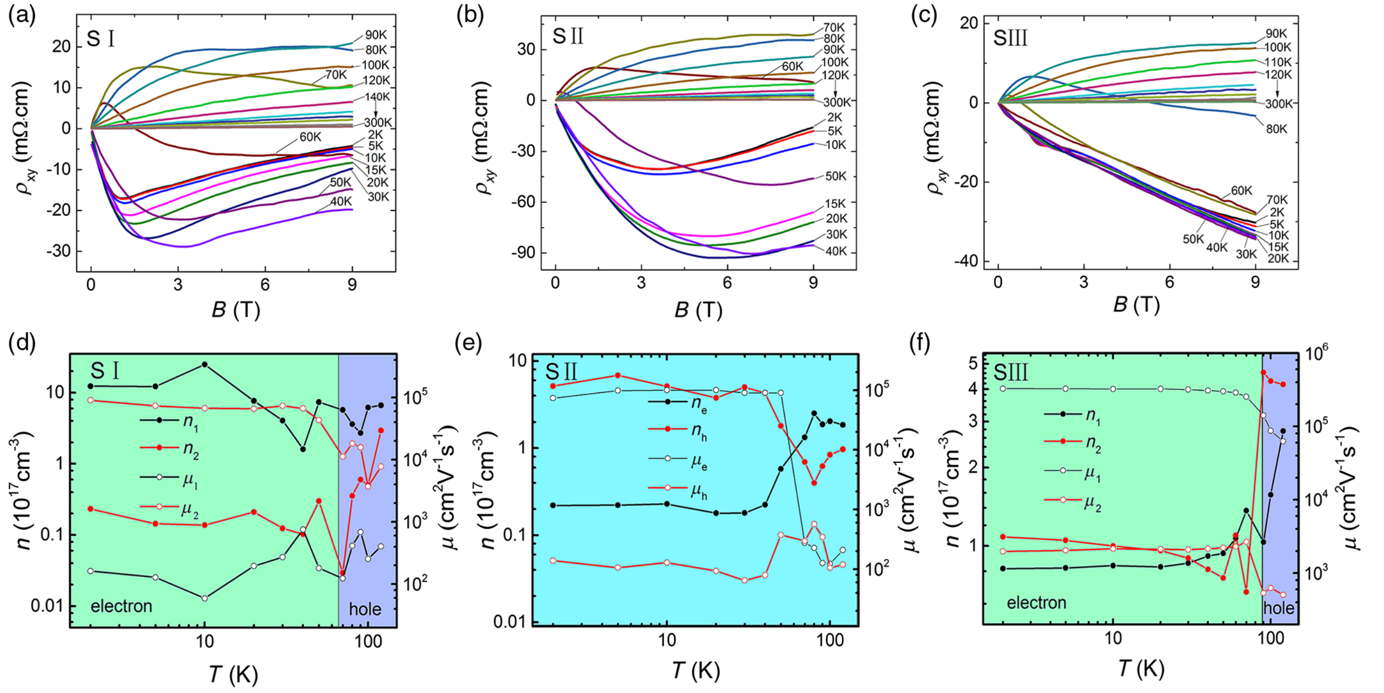

FIG. 4. (a)–(c) The B-dependent Hall resistivity of sample SI ($HfTe_{4.98}$) (a), SII ($HfTe_{4.92}$) (b), and SIII ($HfTe_{4.87}$) (c), measured under a temperature range from 2 to 300 K, respectively. (d)–(f) The temperature-dependent carrier densities and mobility, extracted from the two-carrier-model analysis, of sample SI ($HfTe_{4.98}$) (d), SII ($HfTe_{4.92}$) (e), and SIII ($HfTe_{4.87}$) (f), respectively.

($n_2 = 2.32 \times 10^{16}$ cm^{-3}), and the corresponding mobility is $\mu_1 = 162$ cm^2 V^{-1} s^{-1} ($\mu_2 = 9.03 \times 10^4$ cm^2 V^{-1} s^{-1}). Upon 70 K, both of the two kinds of carriers are changed to hole type. At around 70 K, the electron and hole carrier concentration of the sample $HfTe_{4.98}$ reach nearly compensation. In the sample $HfTe_{4.92}$ [Fig. 4(e)], there is the coexistence of both hole and electron carriers in the measured temperature range. The electron carriers (n_e) have a quite low density of 2.20×10^{16} cm^{-3} and a high mobility (μ_e) of about 7.34×10^4 cm^2 V^{-1} s^{-1} at 2 K, while the hole carriers (n_h) show a higher density of 5.16×10^{17} cm^{-3} but a lower mobility (μ_h) of 140 cm^2 V^{-1} s^{-1}. When the temperature is increased but does not exceed 100 K, both the hole carrier density and electron mobility slightly decrease in magnitude, while both the electron carrier density and hole mobility slightly increase. At around 80 K, the density of hole carriers is approximately equal to the electron carriers, the same as the mobility of hole and electron carriers. And then upon 100 K, the carrier densities grow gradually and the carrier mobility reduces gradually with a temperature increase. The sample $HfTe_{4.87}$ has similar carrier behavior as sample $HfTe_{4.98}$. As present in Fig. 4(f), there are the two kinds of electron carriers with different mobility in the sample $HfTe_{4.87}$ below 90 K. Quantitatively, the carrier density is $n_1 = 8.19 \times 10^{16}$ cm^{-3} ($n_2 = 1.08 \times 10^{17}$ cm^{-3}), and the corresponding mobility is $\mu_1 = 3.28 \times 10^5$ cm^2 V^{-1} s^{-1} ($\mu_2 = 1978$ cm^2 V^{-1} s^{-1}) at 2 K. At around 90 K, the electron carriers change to hole type. Based on a Hall data analysis, the different MR behavior among $HfTe_{4.98}$, $HfTe_{4.92}$, and $HfTe_{4.87}$ can be rationalized. At 2 K, the largest MR in $HfTe_{4.92}$ is coincident to the coexistence of an electron and a hole, as well as high carrier mobility at a low temperature, *which are two key factors leading to the extremely large MR observed in* WTe_2 [9]. As to the maximum MR observed at T_P [see Fig. 3(d)], this is attributed to the coexistence of electron and hole carriers and the high carrier mobility at T_p in these samples. The varied T_P is attributed to the electron concentration difference (equivalent to Te-deficiency concentration) in these samples. Conceptually, Te deficiency introduces the electron carriers in these samples. Under thermal excitation, there are electron-hole pairs generated in a narrow-band semiconductor at a high temperature. At T_P, there are equivalent hole and electron concentrations in $HfTe_{5-\delta}$. Because there is the highest Te deficiency (equivalent electron concentration) in $HfTe_{4.87}$, T_P is the largest, because more thermal energy is needed to excite a high hole concentration, which is obviously shown in Fig. 3(d). Certainly, the above discussion is based on the analysis of the macroscopic transport measurement. The detailed microscopic measurements (like scanning tunneling microscopy and angle-resolved photoemission spectroscopy) should be applied to obtain more information to fully understand the tunable electrical transport behavior in $HfTe_{5-\delta}$ sample.

IV. SUMMARY

In conclusion, we experimentally demonstrate the tunability of the electrical and magnetotransport property of

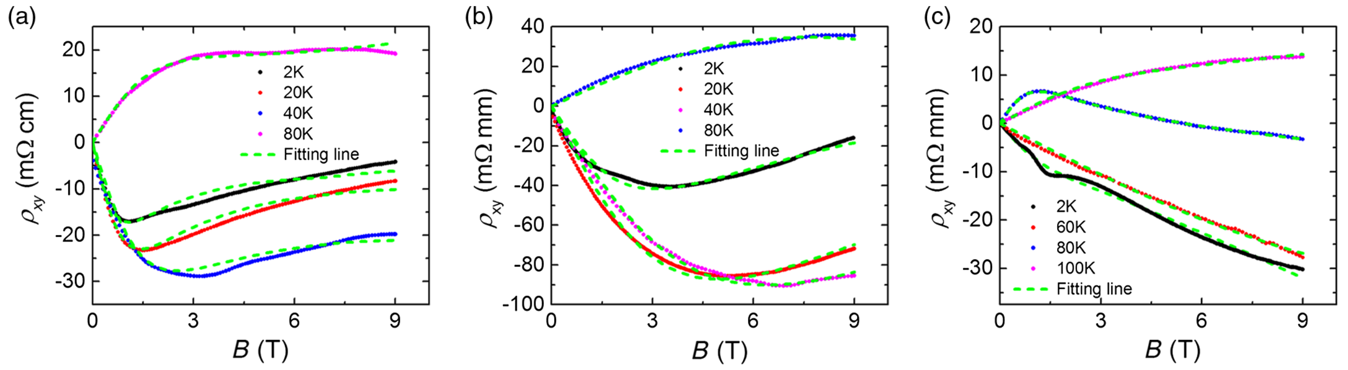

FIG. 5. The representative B-dependent Hall resistivity ρ_{xy} measured at different temperatures and the corresponding fitting curves with the two-carrier model of sample SI ($HfTe_{4.98}$) (a), SII ($HfTe_{4.92}$) (b), and SIII ($HfTe_{4.87}$) (c), respectively. The bright green dashed lines represent the Hall data fitting by the two-carrier model. Obviously, the Hall data can be well fitted by the two-carrier model.

$HfTe_{5-\delta}$ through different excessive amounts of Te during the CVT. The three different kinds of $HfTe_{5-\delta}$ crystals with various Te-deficiency concentrations, Hf∶Te ratios tuned as 1.00∶4.98, 1.00∶4.92, and 1.00∶4.87, are obtained. These $HfTe_{5-\delta}$ crystals show the resistivity cusp at different temperatures [25 ($HfTe_{4.98}$), 51 ($HfTe_{4.92}$), and 72 K ($HfTe_{4.87}$), respectively], as well as the temperatures of the MR peak change from 70 to 90 K in $HfTe_{4.98}$ to $HfTe_{4.87}$. The maximum MR values, measured at 2 K and 9 T magnetic field, are $1.52 \times 10^3\%$, $2.63 \times 10^4\%$, and $6.91 \times 10^3\%$ for sample $HfTe_{4.98}$, $HfTe_{4.92}$, and $HfTe_{4.87}$, respectively. The analysis of the Hall data reveals that there is high carrier mobility and the coexistence of the electron and hole carriers in $HfTe_{4.92}$, which leads to the extremely large magnetoresistance in $HfTe_{4.92}$. Our work demonstrates a successful method to tune the electrical and magnetotransport properties in the $HfTe_5$ single-crystal system, which may be transferable to other transition-metal compounds.

ACKNOWLEDGMENTS

We acknowledge the financial support from the National Basic Research Program of China (973 Program) (2015CB921203 and 2015CB659400), the National Natural Science Foundation of China (51472112, 11574131, 11374140, 11374149, and 9162212), and the Natural Science Foundation of Jiangsu Province, China (BK20171343). Y.-Y. L. acknowledges the financial support from the program A for Outstanding PhD candidate of Nanjing University (201701A008).

APPENDIX: THE HALL DATA FITTING OF $HfTe_{5-\delta}$ SINGLE CRYSTALS

The Hall resistivity ρ_{xy} of $HfTe_{5-\delta}$ single crystals, measured at different temperatures [see Figs. 5(a)–5(c)], show nonlinear behavior, which suggests the relationship between Hall resistivity and B should be analyzed by the classical two-carrier model. All the $\rho_{yx}(= -\rho_{xy})$ data can be fitted to the classical two-band model through the expression

$$\rho_{yx} = \frac{B}{e}\frac{(n_h\mu_h^2 - n_e\mu_e^2) + (n_h - n_e)\mu_h^2\mu_e^2B^2}{(n_h\mu_h + n_e\mu_e)^2 + (n_h - n_e)^2\mu_h^2\mu_e^2B^2}, \quad \text{(A1)}$$

where n_e (or n_h) and μ_e (or μ_h) are the density of electrons (or holes) and the mobility of electrons (or holes), respectively. The representative Hall resistivity ρ_{xy} of $HfTe_{5-\delta}$ single crystals and the corresponding fitting curves are presented in Fig. 5. The temperature-dependent carrier concentration and mobility are displayed in Fig. 4.

[1] M. N. Baibich, J. M. Broto, A. Fert, F. Nguyen Van Dau, F. Petroff, P. Etienne, G. Creuzet, A. Friederich, and J. Chazelas, Giant Magnetoresistance of (001) Fe/(001) Cr Magnetic Superlattices, Phys. Rev. Lett. **61**, 2472 (1988).
[2] A. P. Ramirez, R. J. Cava, and J. Krajewski, Colossal magnetoresistance in Cr-based chalcogenide spinels, Nature (London) **386**, 156 (1997).
[3] F. Y. Yang, K. Liu, K. Hong, D. H. Reich, P. C. Searson, and C. L. Chien, Large magnetoresistance of electrodeposited single-crystal bismuth thin films, Science **284**, 1335 (1999).
[4] Y. Kopelevich, J. H. S. Torres, R. R. da Silva, F. Mrowka, H. Kempa, and P. Esquinazi, Reentrant Metallic Behavior of Graphite in the Quantum Limit, Phys. Rev. Lett. **90**, 156402 (2003).
[5] R. Xu, A. Husmann, T. F. Rosenbaum, M.-L. Saboungi, J. E. Enderby, and P. B. Littlewood, Large magnetoresistance in non-magnetic silver chalcogenides, Nature (London) **390**, 57 (1997).
[6] D.-X. Qu, Y. S. Hor, J. Xiong, R. J. Cava, and N. P. Ong, Quantum oscillations and Hall anomaly of surface states in the topological insulator Bi_2Te_3, Science **329**, 821 (2010).
[7] E. Mun, H. Ko, G. J. Miller, G. D. Samolyuk, S. L. Bud'ko, and P. C. Canfield, Magnetic field effects on transport properties of $PtSn_4$, Phys. Rev. B **85**, 035135 (2012).
[8] H. Takatsu, J. J. Ishikawa, S. Yonezawa, H. Yoshino, T. Shishidou, T. Oguchi, K. Murata, and Y. Maeno, Extremely

Large Magnetoresistance in the Nonmagnetic Metal $PdCoO_2$, Phys. Rev. Lett. **111**, 056601 (2013).

[9] M. N. Ali, J. Xiong, S. Flynn, J. Tao, Q. D. Gibson, L. M. Schoop, T. Liang, N. Haldolaarachchige, M. Hirschberger, N. P. Ong, and R. J. Cava, Large, non-saturating magnetoresistance in WTe_2, Nature (London) **514**, 205 (2014).

[10] K. Wang, D. Graf, L. Li, L. Wang, and C. Petrovic, Anisotropic giant magnetoresistance in $NbSb_2$, Sci. Rep. **4**, 7328 (2014).

[11] F. F. Tafti, Q. D. Gibson, S. K. Kushwaha, N. Haldolaarachchige, and R. J. Cava, Resistivity plateau and extreme magnetoresistance in LaSb, Nat. Phys. **12**, 272 (2016).

[12] F. C. Chen, H. Y. Lv, X. Luo, W. J. Lu, Q. L. Pei, G. T. Lin, Y. Y. Han, X. B. Zhu, W. H. Song, and Y. P. Sun, Extremely large magnetoresistance in the type-II Weyl semimetal $MoTe_2$, Phys. Rev. B **94**, 235154 (2016).

[13] W. S. Gao, N. N. Hao, F.-W. Zheng, W. Ning, M. Wu, X. D. Zhu, G. L. Zheng, J. L. Zhang, J. W. Lu, H. W. Zhang, C. Y. Xi, J. Y. Yang, H. F. Du, P. Zhang, Y. H. Zhang, and M. L. Tian, Extremely Large Magnetoresistance in a Topological Semimetal Candidate Pyrite $PtBi_2$, Phys. Rev. Lett. **118**, 256601 (2017).

[14] T. Liang, Q. Gibson, M. N. Ali, M. Liu, R. J. Cava, and N. P. Ong, Ultrahigh mobility and giant magnetoresistance in the Dirac semimetal Cd_3As_2, Nat. Mater. **14**, 280 (2015).

[15] S. K. Kushwaha, J. W. Krizan, B. E. Feldman, A. Gyenis, M. T. Randeria, J. Xiong, S.-Y. Xu, N. Alidoust, I. Belopolski, T. Liang, M. Zahid Hasan, N. P. Ong, A. Yazdani, and R. J. Cava, Bulk crystal growth and electronic characterization of the 3D Dirac semimetal Na_3Bi, APL Mater. **3**, 041504 (2015).

[16] C. Shekhar, A. K. Nayak, Y. Sun, M. Schmidt, M. Nicklas, I. Leermakers, U. Zeitler, Y. Skourski, J. Wosnitza, Z. Liu, Y. Chen, W. Schnelle, H. Borrmann, Y. Grin, C. Felser, and B. Yan, Extremely large magnetoresistance and ultrahigh mobility in the topological Weyl semimetal candidate NbP, Nat. Phys. **11**, 645 (2015).

[17] X. Huang, L. Zhao, Y. Long, P. Wang, D. Chen, Z. Yang, H. Liang, M. Xue, H. Weng, Z. Fang, X. Dai, and G. Chen, Observation of the Chiral-Anomaly-Induced Negative Magnetoresistance in 3D Weyl Semimetal TaAs, Phys. Rev. X **5**, 031023 (2015).

[18] J. Daughton, J. Brown, E. Chen, R. Beech, A. Pohm, and W. Kude, Magnetic field sensors using GMR multilayer, IEEE Trans. Magn. **30**, 4608 (1994).

[19] J. M. Daughton, GMR applications, J. Magn. Magn. Mater. **192**, 334 (1999).

[20] S. A. Wolf, D. D. Awschalom, R. A. Buhrman, J. M. Daughton, S. von Molnar, M. L. Roukes, A. Y. Chtchelkanova, and D. M. Treger, Spintronics: A spin-based electronics vision for the future, Science **294**, 1488 (2001).

[21] C.-L. Wang, Y. Zhang, J.-W. Huang, G.-D. Liu, A.-J. Liang, Y.-X. Zhang, B. Shen, J. Liu, C. Hu, Y. Ding, D.-F. Liu, Y. Hu, S.-L. He, L. Zhao, L. Yu, J. Hu, J. Wei, Z.-Q. Mao, Y.-G. Shi, X.-W. Jia, F.-F. Zhang, S.-J. Zhang, F. Yang, Z.-M. Wang, Q.-J. Peng, Z.-Y. Xu, C.-T. Chen, and X.-J. Zhou, Evidence of electron-hole imbalance in WTe_2 from high-resolution angle-resolved photoemission spectroscopy, Chin. Phys. Lett. **34**, 097305 (2017).

[22] S. Thirupathaiah, Rajveer Jha, Banabir Pal, J. S. Matias, P. Kumar Das, P. K. Sivakumar, I. Vobornik, N. C. Plumb, M. Shi, R. A. Ribeiro, and D. D. Sarma, $MoTe_2$: An uncompensated semimetal with extremely large magnetoresistance, Phys. Rev. B **95**, 241105(R) (2017).

[23] T. Zandt, H. Dwelk, C. Janowitz, and R. Manzke, Quadratic temperature dependence up to 50 K of the resistivity of metallic $MoTe_2$, J. Alloys Compd. **442**, 216 (2007).

[24] J. F. He, C. F. Zhang, N. J. Ghimire, T. Liang, C. J. Jia, J. Jiang, S. J. Tang, S. D. Chen, Y. He, S.-K. Mo, C. C. Hwang, M. Hashimoto, D. H. Lu, B. Moritz, T. P. Devereaux, Y. L. Chen, J. F. Mitchell, and Z.-X. Shen, Distinct Electronic Structure for the Extreme Magnetoresistance in YSb, Phys. Rev. Lett. **117**, 267201 (2016).

[25] S. Furuseth, L. Brattas, and A. Kjekshus, The crystal structure of $HfTe_5$, Acta Chem. Scand. **27**, 2367 (1973).

[26] F. J. DiSalvo, R. M. Fleming, and J. V. Waszczak, Possible phase transition in the quasi-one-dimensional materials $ZrTe_5$ or $HfTe_5$, Phys. Rev. B **24**, 2935 (1981).

[27] E. F. Skelton, T. J. Wieting, S. A. Wolf, W. W. Fuller, D. U. Gubser, and T. L. Francavilla, Giant resistivity and x-ray diffraction anomalies in low-dimensional $ZrTe_5$ and $HfTe_5$, Solid State Commun. **42**, 1 (1982).

[28] M. Izumi, K. Uchinokura, S. Harada, R. Yoshizaki, and E. Matsuura, Strong resistivity anomaly in a new low-dimensional conductor $HfTe_5$, Mol. Cryst. Liq. Cryst. **81**, 141 (1982).

[29] M. Izumit, T. Nakayama, K. Uchinokura, S. Harada, R. Yoshizaki, and E. Matsuura, Shubnikov-de Haas oscillations and Fermi surfaces in transition-metal pentatellurides $ZrTe_5$ and $HfTe_5$, J. Phys. C **20**, 3691 (1987).

[30] G. N. Kamm, D. J. Csillespie, A. C. Ehrlich, D. L. Peebles, and F. Levy, Fermi surface, effective masses, and energy bands of $Hfre_5$ as derived from the Shubnikov-de Haas effect, Phys. Rev. B **35**, 1223 (1987).

[31] T. E. Jones, W. W. Fuller, T. J. Wieting, and F. Levy, Thermoelectric power of $HfTe_5$ and $ZrTe_5$, Solid State Commun. **42**, 793 (1982).

[32] N. D. Lowhorn, T. M. Tritt, E. E. Abbott, and J. W. Kolis, Enhancement of the power factor of the transition metal pentatelluride $HfTe_5$ by rare-earth Doping, Appl. Phys. Lett. **88**, 022101 (2006).

[33] H. M. Weng, X. Dai, and Z. Fang, Transition-Metal Pentatelluride $ZrTe_5$ and $HfTe_5$: A Paradigm for Large-Gap Quantum Spin Hall Insulators, Phys. Rev. X **4**, 011002 (2014).

[34] Z. J. Fan, Q.-F. Liang, Y. B. Chen, S.-H. Yao, and J. Zhou, Transition between strong and weak topological insulator in $ZrTe_5$ and $HfTe_5$, Sci. Rep. **7**, 45667 (2017).

[35] Y. Zhang, C. L. Wang, G. D. Liu, A. J. Liang, L. X. Zhao, J. W. Huang, Q. Gao, B. Shen, J. Liu, C. Hu, W. J. Zhao, G. F. Chen, X. W. Jia, L. Yu, L. Zhao, S. L. He, F. F. Zhang, S. J. Zhang, F. Yang, Z. M. Wang, Q. J. Peng, Z. Y. Xu, C. T. Chen, and X. J. Zhou, Temperature-induced Lifshitz transition in topological insulator candidate $HfTe_5$, Science Bulletin **62**, 950 (2017).

[36] L.-X. Zhao, X.-C. Huang, Y.-J. Long, D. Chen, H. Liang, Z.-H. Yang, M.-Q. Xue, Z.-A. Ren, H.-M. Weng, Z. Fang, X. Dai, and G.-F. Chen, Anomalous magneto-transport

behavior in transition metal pentatelluride $HfTe_5$, Chin. Phys. Lett. **34**, 037102 (2017).

[37] Y. P. Qi, W. J. Shi, P. G. Naumov, N. Kumar, W. Schnelle, O. Barkalov, C. Shekhar, H. Borrmann, C. Felser, B. H. Yan, and S. A. Medvedev, Pressure-driven superconductivity in the transition-metal pentatelluride $HfTe_5$, Phys. Rev. B **94**, 054517 (2016).

[38] Y. Liu, Y. J. Long, L. X. Zhao, S. M. Nie, S. J. Zhang, Y. X. Weng, M. L. Jin, W. M. Li, Q. Q. Liu, Y. W. Long, R. C. Yu, C. Z. Gu, F. Sun, W. G. Yang, H. K. Mao, X. L. Feng, Q. Li, W. T. Zheng, H. M. Weng, X. Dai, Z. Fang, G. F. Chen, and C. Q. Jin, Superconductivity in $HfTe_5$ across weak to strong topological insulator transition induced via pressures, Sci. Rep. **7**, 44367 (2017).

[39] H. C. Wang, C.-K. Li, H. W. Liu, J. Q. Yan, J. F. Wang, J. Liu, Z. Q. Lin, Y. Li, Y. Wang, L. Li, D. Mandrus, X. C. Xie, J. Feng, and J. Wang, Chiral anomaly and ultrahigh mobility in crystalline $HfTe_5$, Phys. Rev. B **93**, 165127 (2016).

[40] N. Kumar, C. Shekhar, M. X. Wang, Y. L. Chen, H. Borrmann, and C. Felser, Large out-of-plane and linear in-plane magnetoresistance in layered hafnium pentatelluride, Phys. Rev. B **95**, 155128 (2017).

[41] S. Okada, T. Sambongi, M. Ido, Y. Tazuke, R. Aoki, and O. Fujita, Negative evidences for charge/spin density wave in $ZrTe_5$, J. Phys. Soc. Jpn. **51**, 460 (1982).

[42] H. Fjellvag and A. Kjekshus, Structural properties of $ZrTe_5$ and $HfTe_5$ as seen by powder diffraction, Solid State Commun. **60**, 91 (1986).

[43] M. Rubinstein, $HfTe_5$ and $ZrTe_5$: Possible polaronic conductors, Phys. Rev. B **60**, 1627 (1999).

[44] P. Shahi, D. J. Singh, J. P. Sun, L. X. Zhao, G. F. Chen, J.-Q. Yan, D. G. Mandrus, and J.-G. Cheng, Bipolar conduction is the origin of the electronic transition in pentatellurides: Metallic vs. semiconducting behavior, arXiv:1611.06370.

[45] G. L. Zheng, X. D. Zhu, Y. Q. Liu, J. W. Lu, W. Ning, H. W. Zhang, W. S. Gao, Y. Y. Han, J. Y. Yang, H. F. Du, K. Yang, Y. H. Zhang, and M. L. Tian, Field-induced topological phase transition from a three-dimensional Weyl semimetal to a two-dimensional massive Dirac metal in $ZrTe_5$, Phys. Rev. B **96**, 121401(R) (2017).

[46] W. Yu, Y. Jiang, J. Yang, Z. L. Dun, H. D. Zhou, Z. Jiang, P. Lu, and W. Pan, Quantum oscillations at integer and fractional Landau level indices in single-crystalline $ZrTe_5$, Sci. Rep. **6**, 35357 (2016).

[47] J. M. Ziman, *Electrons and Phonons—The Theory of Transport Phenomena in Solids* (Oxford University, New York, 1960), pp. 490–495.

[48] H. Chi, C. Zhang, G. D. Gu, D. E Kharzeev, X. Dai, and Q. Li, Lifshitz transition mediated electronic transport anomaly in bulk $ZrTe_5$, New J. Phys. **19**, 015005 (2017).